Review of Scientific Instruments

Charge exchange spectroscopy using spatial heterodyne spectrometer in the large helical device

Cite as: Rev. Sci. Instrum. **93**, 033503 (2022); https://doi.org/10.1063/5.0078417
Submitted: 12 November 2021 • Accepted: 09 February 2022 • Published Online: 09 March 2022

F. J. Arellano, M. Yoshinuma and K. Ida

View Online Export Citation CrossMark

ARTICLES YOU MAY BE INTERESTED IN

An in situ stretching instrument combined with low field nuclear magnetic resonance (NMR): Rheo-Spin NMR
Review of Scientific Instruments **93**, 033905 (2022); https://doi.org/10.1063/5.0080767

Damage detection of carbon fiber reinforced polymer composite materials based on one-dimensional multi-scale residual convolution neural network
Review of Scientific Instruments **93**, 034701 (2022); https://doi.org/10.1063/5.0076826

A filter-based Raman spectrometer for non-invasive imaging of atmospheric water vapor
Review of Scientific Instruments **93**, 035102 (2022); https://doi.org/10.1063/5.0078784

Lock-in Amplifiers up to 600 MHz
Zurich Instruments
Watch

© 2022 Author(s).

Review of Scientific Instruments ARTICLE scitation.org/journal/rsi

Charge exchange spectroscopy using spatial heterodyne spectrometer in the large helical device

Cite as: Rev. Sci. Instrum. 93, 033503 (2022); doi: 10.1063/5.0078417
Submitted: 12 November 2021 • Accepted: 9 February 2022 •
Published Online: 9 March 2022

View Online Export Citation CrossMark

F. J. Arellano,[1] M. Yoshinuma,[2] and K. Ida[2,3,a)]

AFFILIATIONS

[1] Center for Atomic and Molecular Technologies, Osaka University, 2-1 Yamadaoka, Suita, Osaka 565-0871, Japan
[2] National Institute for Fusion Science, 322-6 Oroshi-cho, Toki 502-5292, Japan
[3] The Graduate University for Advanced Studies, SOKENDAI, 322-6 Oroshi-cho, Toki 502-5292, Japan

[a)] **Author to whom correspondence should be addressed:** ida.katsumi@nifs.ac.jp

ABSTRACT

In this study, the use of a spatial heterodyne spectrometer (SHS) to measure the toroidal flow velocity (V_f) and the ion temperature ($T_{C^{6+}}$) of the C^{6+} impurity ion by charge exchange spectroscopy was explored. The instrumental width (IW) of the SHS (aperture size = 16.77 mm^2, etendue = 2.9867 mm$^2 sr$) was extrapolated to be 0.09 nm, which is half of the 0.17 nm IW extrapolated for a conventionally used dispersive spectrometer (DS) (aperture size = 2.6 mm^2, etendue = 0.2605 mm$^2 sr$). The resulting V_f and $T_{C^{6+}}$ measurements were found to be in good agreement with those measured using the DS.

Published under an exclusive license by AIP Publishing. https://doi.org/10.1063/5.0078417

I. INTRODUCTION

The carbon impurity ion temperature ($T_{C^{6+}}$) and the toroidal flow velocity (V_f) in the Large Helical Device (LHD) are typically measured by charge exchange spectroscopy (CXS) using a traditional dispersive spectrometer (DS).[1–3] One disadvantage of employing a DS for CXS is the limitation of the aperture size in order to maintain a high spectral resolution. In a DS, as the input aperture size increases to collect more photons, the spectral resolution becomes significantly poorer. In contrast, a spatial heterodyne spectrometer (SHS) has the advantage of having field-widening prisms that rotate the image of the gratings such that it appears perpendicular to the optical axis and coincident at the output, allowing for a larger aperture size.[4,5] If the SHS is used, one can increase the number of photons collected without significantly degrading the spectral resolution.

The SHS is an interferometric Fourier transform technique, wherein the measured Fizeau fringe patterns are transformed into spectra by Fast Fourier Transform (FFT). It was originally designed for and mainly used in the measurement of emission lines in astrophysics.[5,6] However, in 2018, Burke *et al.* reported the possibility of using an SHS to measure the Stark split neutral beam emissions.[7] In a similar way, the use of SHS as a new technique for CXS can therefore be explored. In this study, the potential of using the SHS for CXS in order to achieve a higher optical transmission-to-spectral resolution ratio is investigated. This can be a great advantage in the measurement of the transient (< 1 ms) deviation of the ion velocity distribution from the Maxwell–Boltzmann distribution that occurs during MHD events.[8]

CXS is characterized by the charge transfer from the impurity ions in the plasma to the neutral atoms coming from the neutral beam, leaving the impurity ion in the excited state.[9] For a fully ionized carbon, this reaction is given by

$$H^0_{beam} + C^{6+} \rightarrow H^+ + C^{5+}(n = 8). \quad (1)$$

The spontaneous emission of the excited impurity ion given by C^{5+} (n = 8 → 7) emits light at λ = 529.05 nm. This emitted radiation can then be measured by the spectrometer. From the Doppler broadening and Doppler shift of the spectral line, the $T_{C^{6+}}$ and the V_f can be calculated.

Published under an exclusive license by AIP Publishing

II. EXPERIMENTAL SETUP

A. SHS in LHD

Figure 1(a) shows the schematic view of the LHD with the line-of-sight (LOS) of the DS and SHS systems. The LHD is a heliotron device consisting of three tangential beams (NB#1–NB#3) and two perpendicular beams (NB#4 and NB#5). The SHS is connected to the lens located at the viewing port 9-O. Neutral beam NM#5, which is located at port 1-O, is used to induce the charge exchange reaction corresponding to the SHS measurements. NB#5 is oriented perpendicular to the magnetic flux surface along the major radius. Using mirrors, the LOS of the lens at port 9-O was arranged such that it intersected with NB#5 at an angle of 113.6°. The intersecting region spans from the magnetic axis to the outboard edge of the LHD plasma. However, in this study, SHS measurements were only done in the portion of the intersecting region near the magnetic axis, that is, at R = 3.66 m. The SHS was placed on an anti-vibration table to increase resilience to vibrations.

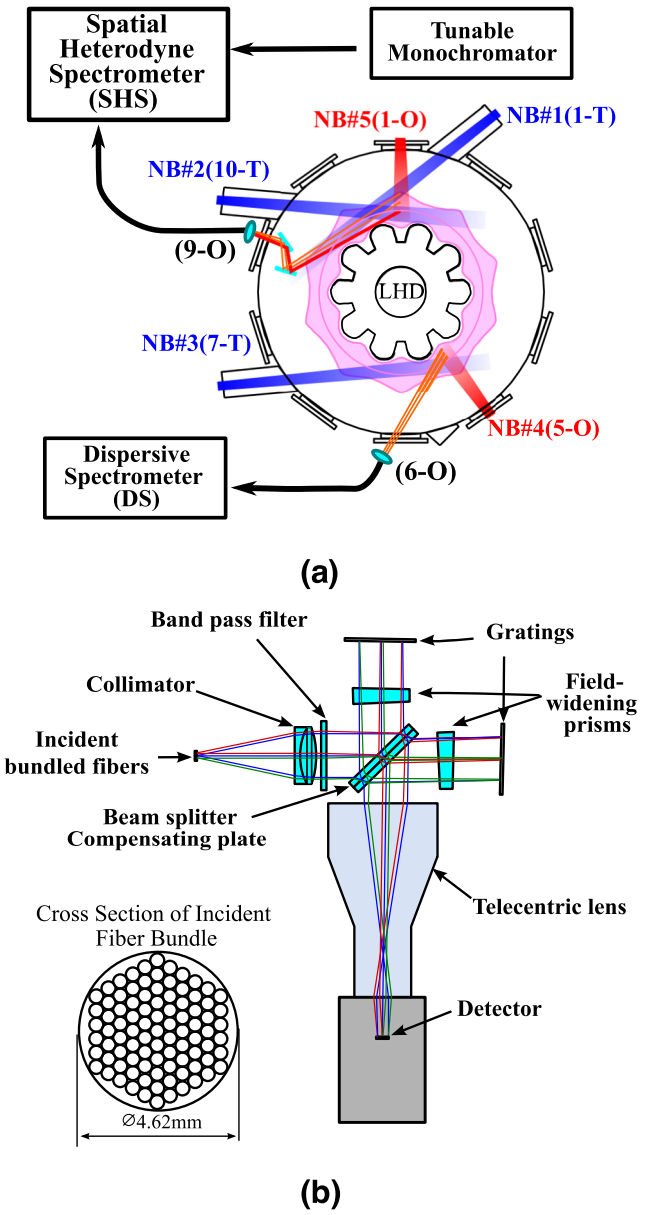

FIG. 1. (a) SHS and DS configuration in the LHD and (b) the schematic diagram of SHS.

Charge exchange between fully ionized carbons and thermal neutrals in the plasma produces light emission that overlaps the wavelength range of the target emission. To measure the background emission coming from this charge exchange with the thermal neutrals, NB#5 was modulated on and off. The background emission corresponded to the intensity measured when the beam was off.

For comparison purposes, the intensity of the charge exchange line collected using a DS (Bunkoukeiki Co., Ltd., CLP-400) was also measured. The DS is located at port 6-O, wherein the neutral beam CXS (NBCXS) is induced by NB#4. The LOS of the DS intersects with the NB#4 at an angle of 103°. Similar to the SHS measurements, the DS measurements used in this study were those measured at R = 3.66 m.

B. Spatial heterodyne spectrometer

The setup of an SHS is fundamentally similar to a Michelson interferometer, but with diffraction gratings instead of mirrors. A schematic diagram of the SHS (Bunkoukeiki Co., Ltd., BSH-529P) used in this experiment is shown in Fig. 1(b).

The light collected by the lens at the LHD port 9-O is directed to the SHS fiber bundle. This fiber bundle contains 91 fiber cores with a bundle diameter of 4.62 mm. The divergent incident light is then collimated by an achromatic collimator lens and guided to a three-cavity band pass filter centered at 529.0 nm. After that, the light beam is split into two by the beam splitter, and the resulting beams are directed to the two gratings. The synthetic quartz compensating plate on the beam splitter was compensated for the variation of optical path induced in one arm. Field widening prisms are inserted between the splitter and the gratings. Upon reaching the gratings, light is diffracted at an angle that is dependent on the wavelength. At a wavelength called the Littrow wavelength, light is returned to the same direction of incidence. The angle of the tilt of the gratings with respect to the optical axis is called the Littrow angle. The SHS used in this study has a tunable Littrow wavelength.

On the way to the detector, light is made to pass through a telecentric lens to reduce perspective errors. For each wavelength that goes through the filter, two wavefronts with a wavelength-dependent crossing angle in between them reach the detector. The superposition of these two wavefronts leads to the formation of a Fizeau fringe pattern. The spatial frequency of the Fizeau pattern is dependent on the corresponding wavelength.

C. SHS calibration

To calibrate the SHS, the intensity of the light coming from a tunable wavelength monochromatic light source (TLS) was measured and transformed into spectra. The wavelength of the TLS was tuned from 527 to 530.8 nm. The spectrum linewidth of the monochromatic light can be varied by changing the width of the exit

Published under an exclusive license by AIP Publishing

slit of the TLS. Figures 2(a)–2(c) show the Fizeau fringe image produced at the detector from the light at 528, 529, and 530 nm. Here, the spatial frequency of the fringe patterns is observed to decrease with increasing wavelength. The spectra given in Fig. 2(d) are then derived from the FFT of these fringe patterns. It can be observed from Fig. 2(d) that distinct peaks were successfully measured at each specific wavelength value. A zero spatial frequency was measured at 530.8 nm, setting it as the Littrow wavelength.

D. Instrumental width (IW)

The spectral resolution of a spectrometer can be characterized by a parameter called the instrumental width (IW). IW is defined to be the FWHM of the instrumental line profile (ILP).

In this study, the full width at half maximum (FWHM) of the ILP is measured for both the SHS and the DS by adjusting the spectrum linewidth of the light from the TLS at 529 nm. A single optical fiber is used to transfer the light from the TLS to the SHS and DS. The IW is extrapolated to be the value of the FWHM when the spectrum linewidth is zero and is given in Fig. 3 for both spectrometers.

In Fig. 3, the FWHM measured using the DS and the SHS are plotted along with its line of best fit. The almost linear behavior of the fitted line shows a good agreement between the FWHM measured from both spectrometers. Therefore, the SHS has the ability to measure the FWHM correctly as well as a DS does. The IW of the SHS was extrapolated to be 0.09 nm, which is almost half of that of the DS (IW = 0.17 nm). Comparing the optical transmission of the two optical systems, the aperture size of the SHS and the DS are calculated to be 16.77 and 2.6 mm^2, respectively. Another way to express the optical transmission is through a parameter called etendue (G), which is calculated by

$$G = S\sigma = S\frac{\pi}{4F^2}, \tag{2}$$

where S is the aperture size, σ is the solid angle, and F is the F-number. The F-number of the SHS and the DS are 2.1 and 2.8, respectively. The values of the etendue of the SHS and the DS are therefore calculated to be 2.9867 and 0.2605 mm^2sr, respectively. These significant differences in the etendue and the instrumental width presents the SHS as a suitable instrument for measurements requiring high spectral resolution and high optical transmission.

III. RESULTS AND DISCUSSION

SHS and DS measurements were done using Shot No. 164208 of the LHD. Figure 4 shows the discharge characteristics of this shot. The first inset shows the beam power of the neutral beams. Here, "NB#1–NB#3" is the sum of the power from neutral beams 1–3. NB#4, NB#5, and ECH represent the power from NB#4, NB#5, and the electron cyclotron heating (ECH), respectively. It can be seen that during beam modulation, NB#4 and NB#5 were turned on for a longer duration than they were turned off. This allowed for more time-resolved data of the ion parameters. The second inset shows the power of the NB#5 plotted alongside the time-dependent intensity derived from the SHS interferogram after FFT. The intensity values were calculated by integrating the spectra from 528.5 to 529.7 nm. This shows how the intensity is directly proportional to the NB#5 power. The third and fourth insets show the $T_{C^{6+}}$, the electron temperature (T_e), and the electron density (n_e). Here, the T_e and the n_e

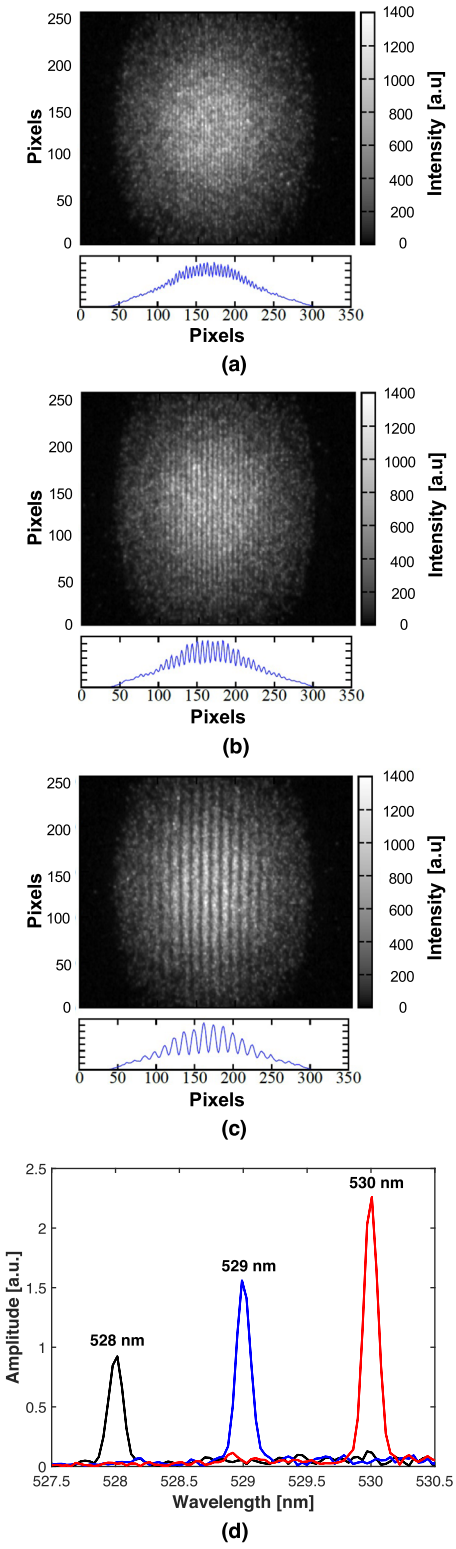

FIG. 2. (a)–(c) Measured fringe patterns and (d) derived spectra from SHS calibration using a tunable monochromatic light source.

Published under an exclusive license by AIP Publishing

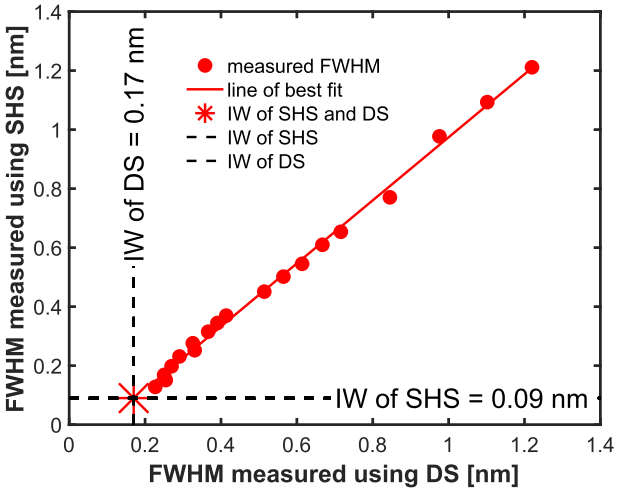

FIG. 3. FWHM measured with the SHS and the DS along with the instrumental width (IW) values.

were measured by Thomson scattering, while the $T_{C^{6+}}$ was measured using the DS. The T_e and $T_{C^{6+}}$ are observed to increase and decrease following the ECH modulation.

Figure 5 shows the resulting SHS interferogram and spectra from Shot No. 164208. Measurements were taken at t = 3.4 s

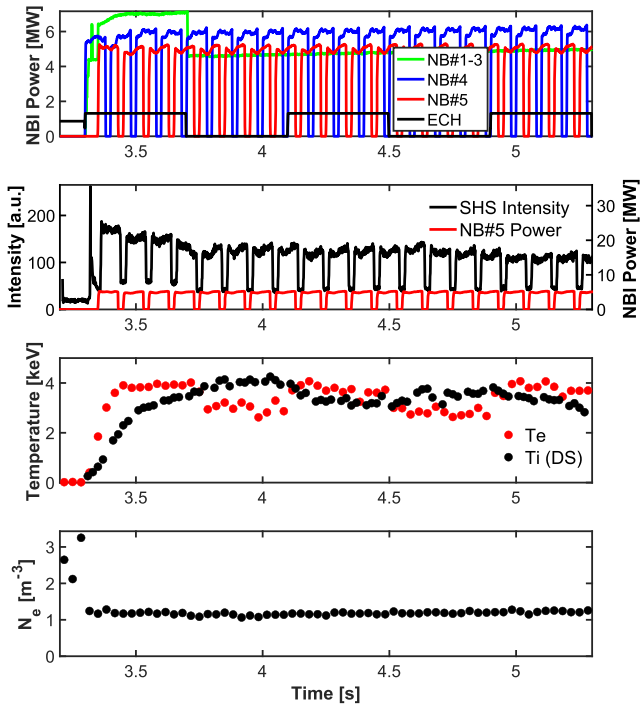

FIG. 4. Parameters of LHD Shot No. 164208.

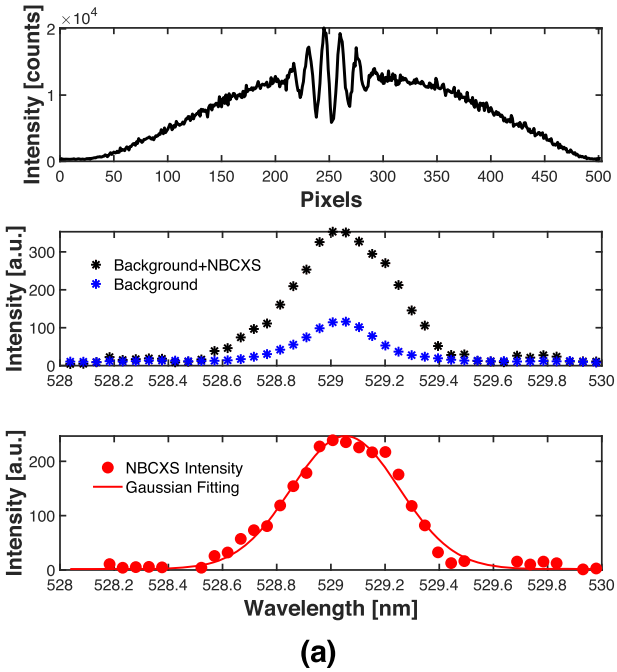

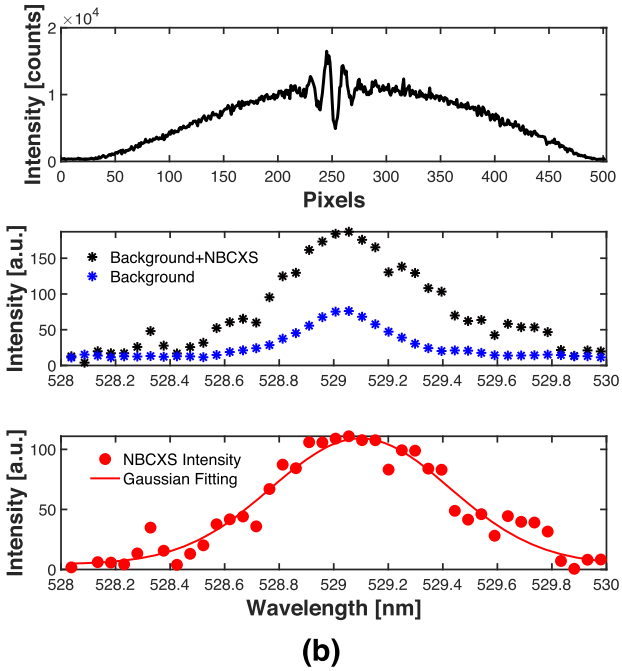

FIG. 5. SHS signal and spectra at (a) t = 3.4 s ($T_{C^{6+}}$ = 2.76 keV) and (b) t = 4.0 s ($T_{C^{6+}}$ = 4.38 keV).

[Fig. 5(a)] and t = 4.0 s [Fig. 5(b)]. The first insets show the raw interferograms directly measured from the SHS. The second insets show the intensity derived after FFT ("Background + NBCXS"), along with the background emission ("Background"). The background

Published under an exclusive license by AIP Publishing

emission is calculated by interpolating the neighboring time frames when the NB#5 was turned off. This background emission is then subtracted from the raw intensity to get the CXS intensity induced by NB#5 ("NBCXS Intensity") shown in the third insets. The resulting spectra are then fitted to a Gaussian curve.

The Gaussian fit of a spectrum is represented by

$$F(\lambda) = I \exp\left[-\frac{(\lambda - \lambda_p)^2}{w^2}\right] + A, \tag{3}$$

where I is the height of the spectrum peak, λ is the corresponding wavelength, λ_p is the peak position, w is the width of the Gaussian curve, and A is the vertical offset from 0. Non-linear least square fitting was done in order to fit the values of I, λ_p, w, and A into Eq. (3). V_f and $T_{C^{6+}}$ can then be calculated from the resulting λ_p and w values. The distance of the λ_p from the standard charge exchange line peak (λ_C) at 529.05 nm yields the Doppler shift. From this value, V_f can be calculated using

$$V_f = c\frac{|\lambda_p - \lambda_C|}{\lambda_C}, \tag{4}$$

where c is the speed of light.

Similarly, w gives the width of the spectrum after Doppler broadening. From this width value, the $T_{C^{6+}}$ is calculated using

$$T_{C^{6+}} = \frac{Am_p[(w^2 - w_{SHS}^2)^{0.5} c/\lambda_C]^2}{2}, \tag{5}$$

where A is the atomic mass of carbon, m_p is the proton mass, and w_{SHS} is the Gaussian width induced by instrumental broadening. w_{SHS} is directly related to the instrumental width (IW) calculated in Sec. II D. However, in the case of the w_{SHS}, instead of using the FWHM, the half-width at the height of e^{-1} is used. w_{SHS} is therefore calculated from the IW using

$$w_{SHS} = \frac{IW}{2\sqrt{ln2}}. \tag{6}$$

In Fig. 5, the measurements from t = 3.4 s and t = 4.0 s were taken because the calculated $T_{C^{6+}}$ is observed to be lowest at t = 3.4 s and highest at t = 4.0 s. Actually, if the figure is looked into closer, one can see that the relative level of the $T_{C^{6+}}$ can already be observed even from the interferogram given on the first inset of Figs. 5(a) and 5(b). Higher sine wave modulation (given at the peak of the interferogram) is present when a lower Doppler width is measured (t = 3.4 s), while a lower sine wave modulation is present at a higher Doppler width (t = 4.0 s). The Doppler width is then observed more clearly after FFT, shown by the width of the spectral line in the second and third insets. This observation allows for a relative guess of the $T_{C^{6+}}$ even just from the measured interferograms.

Wavelength values for the derived spectrum are then calculated using

$$\frac{1}{\lambda}[nm^{-1}] = \left(\frac{M\sigma_D}{4\tan\theta - (8\tan\beta_i/n\sigma_0)(dn/d\lambda)} + \sigma_0\right) \times 10^7, \tag{7}$$

where M is the magnification of the telecentric lens, σ_D is the spatial frequency of the waveform (in mm^{-1}), σ_0 is the Littrow wavenumber corresponding to the Littrow wavelength λ_0, n is the refractive index of the grating at λ_0, β_i is the angle of incidence, and $dn/d\lambda$ is the rate of change of the refractive index at λ_0. The resulting SHS spectrum is shown in Fig. 6(a) and is plotted along with that of the DS. Here, the SHS and the DS spectra are both passive and were taken at a pulse around t = 4.0 s from another LHD shot (Shot No. 163968). From this figure, it can be seen that the peaks of the SHS and DS spectra do not match. The Littrow wavelength used in Eq. (7) is therefore adjusted in such a way that the SHS peaks matched those of the DS, resulting in the figure given in Fig. 6(b). Here, the Littrow wavelength of 530.8 nm measured from the calibration is adjusted to 530.66 nm to match the peaks. The Littrow angle for Eq. (7) is then calculated from this new Littrow wavelength value using

$$\theta = \sin^{-1}\left(\frac{N\lambda_0}{2}\right), \tag{8}$$

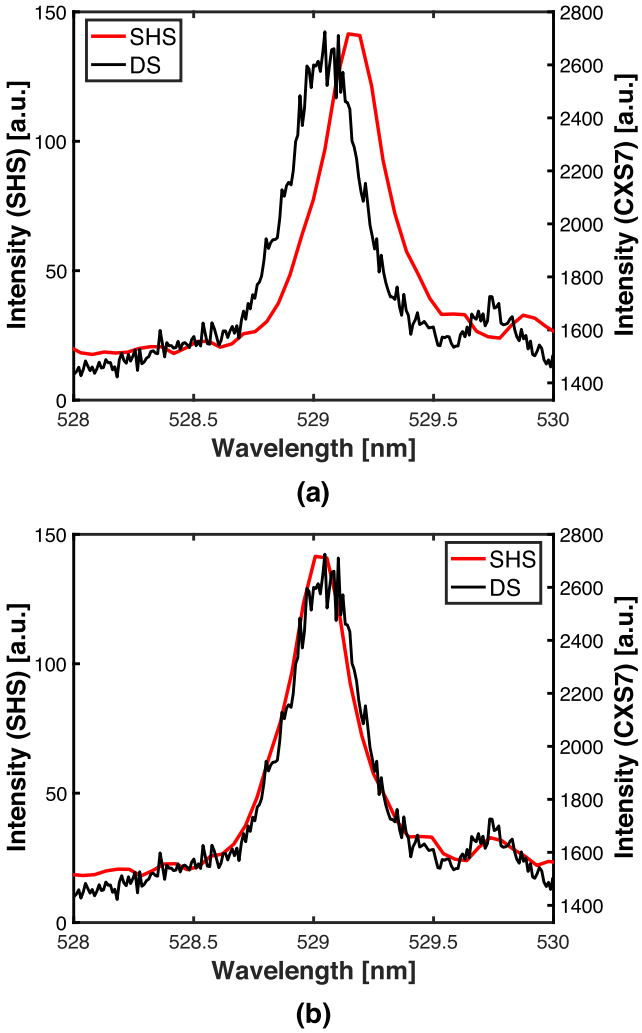

FIG. 6. SHS and DS spectra (a) before adjustment (λ_0 = 530.8 nm) and (b) after adjustment (λ_0 = 530.66 nm).

Published under an exclusive license by AIP Publishing

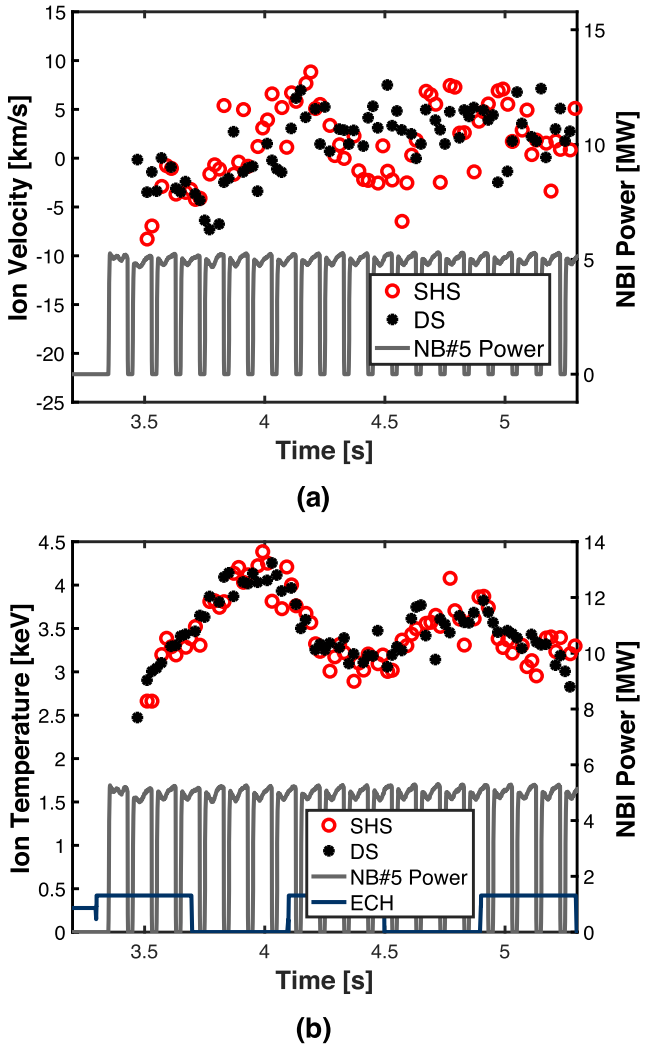

FIG. 7. (a) Toroidal flow velocity (V_f) and (b) carbon impurity ion temperature ($T_{C^{6+}}$).

where N is the grating groove density. This discrepancy in the peak position is attributed to the changes in the Littrow wavelength caused by environmental temperature and pressure changes.

Wavelength adjustment was chosen to be done in such a manner due to the sensitivity of the SHS to environmental conditions. Although the SHS and the DS are measuring the toroidal flow from opposite directions, the position of the DS peak shows that the Doppler shift due to the cold component is <0.01 nm, which is small compared to the 0.14 nm adjustment applied on SHS spectra.

Figure 7 shows the resulting time-dependent V_f and $T_{C^{6+}}$ values, along with the values measured from the DS. The V_f and $T_{C^{6+}}$ values from the SHS are averaged for every 20 ms interval. It can be observed that the resulting $T_{C^{6+}}$ measured from the SHS has the same trend and is in good agreement with that measured using the DS. Both $T_{C^{6+}}$ measurements show the alternating high-low temperature that went with the ECH modulation. In the case of V_f, values measured from the SHS and DS are observed to be scattered, but the two measurements are found to be in the same range and same general trend. This good agreement shows how the SHS can be used for CXS measurements with the advantage of having a higher resolution at higher optical transmission than a traditional DS.

IV. CONCLUSION

In this study, charge exchange spectroscopy (CXS) in the Large Helical Device (LHD) is performed using a spatial heterodyne spectrometer (SHS) in order to achieve higher spectral resolution even at higher optical transmission. To characterize the spectral resolution, the instrumental width (IW) of the SHS is measured and compared to that of a traditional dispersive spectrometer (DS). The instrumental width of the SHS (IW = 0.09 nm) is extrapolated to be almost half of that of the DS (IW = 0.17 nm) even though the SHS (aperture size = 16.77 mm^2, etendue = 2.9867 mm^2*sr*) has a higher optical transmission than the DS (aperture size = 2.6 mm^2, etendue = 0.2605 mm^2*sr*). Additionally, the SHS was used to measure the toroidal flow velocity (V_f) and the ion temperature ($T_{C^{6+}}$) of the C^{6+} impurity present in the LHD. The interferogram measured from the SHS is transformed into spectra using Fourier transform. V_f and $T_{C^{6+}}$ are then calculated from the Doppler shift and Doppler width of the Gaussian fitting of the spectra derived. The calculated V_f and $T_{C^{6+}}$ are shown to be in good agreement with the values measured using the DS.

ACKNOWLEDGMENTS

The authors would like to thank the LHD experiment group for their excellent support in this work. This work was supported by Grants-in-Aid for Scientific Research (Grant No. 21H04973 to K.I.) of the Japan Society for the Promotion of Science (JSPS).

F.J. Arellano would like to thank Professor Satoshi Hamaguchi (Osaka University) and the Japan International Cooperation Agency (JICA) Innovative Asia Program for the collaboration opportunity with the National Institute of Fusion Science (NIFS).

AUTHOR DECLARATIONS

Conflict of Interest

The authors have no conflicts of interest to disclose.

DATA AVAILABILITY

The data that support the findings of this study are openly available in the LHD Experiment Data Repository.[10]

REFERENCES

[1]T. Ito, M. Osakabe, K. Ida, M. Yoshinuma, M. Kobayashi, M. Goto, S. Murakami, M. Isobe, S. Kobayashi, K. Toi *et al.*, Rev. Sci. Instrum. **81**, 10D327 (2010).

[2]W.-H. Ko, H. Lee, D. Seo, and M. Kwon, Rev. Sci. Instrum. **81**, 10D740 (2010).

Published under an exclusive license by AIP Publishing

[3]M. Yoshinuma, K. Ida, M. Yokoyama, M. Osakabe, and K. Nagaoka, Fusion Sci. Technol. **58**, 375–382 (2010).
[4]M. Kaufmann, F. Olschewski, K. Mantel, O. Wroblowski, Q. Chen, J. Liu, Q. Gong, D. Wei, Y. Zhu, T. Neubert *et al.*, CEAS Space J. **11**, 525–531 (2019).
[5]J. Harlander, R. J. Reynolds, and F. L. Roesler, Astrophys. J. **396**, 730–740 (1992).
[6]J. M. Harlander and F. L. Roesler, Proc. SPIE **1235**, Instrumentation in Astronomy VII (1 July 1990).
[7]M. G. Burke, R. J. Fonck, G. R. McKee, and G. R. Winz, Rev. Sci. Instrum. **89**, 10D114 (2018).
[8]K. Ida, T. Kobayashi, M. Yoshinuma, T. Akiyama, T. Tokuzawa, H. Tsuchiya, K. Itoh, and L. E. Group, Phys. Plasmas **24**, 122502 (2017).
[9]R. C. Isler, Plasma Phys. Controlled Fusion **36**, 171–208 (1994).
[10]See https://www-lhd.nifs.ac.jp/pub/Repository_en.html for LHD Experiment Data Repository.

Published under an exclusive license by AIP Publishing